

GTC/CANARICAM MID-IR IMAGING OF THE FULLERENE-RICH PLANETARY NEBULA IC 418: SEARCHING FOR THE SPATIAL DISTRIBUTION OF FULLERENE-LIKE MOLECULES

J. J. DÍAZ-LUIS,^{1,2,3} D. A. GARCÍA-HERNÁNDEZ,^{1,2} A. MANCHADO,^{1,2,4} P. GARCÍA-LARIO,⁵ E. VILLAYER,⁶ AND
G. GARCÍA-SEGURA⁷

¹*Instituto de Astrofísica de Canarias, C/ Via Láctea s/n, E-38205 La Laguna, Spain*

²*Departamento de Astrofísica, Universidad de La Laguna (ULL), E-38206 La Laguna, Spain*

³*Observatorio Astronómico Nacional (IGN), Alfonso XII, 3 y 5, 28014 Madrid, Spain*

⁴*Consejo Superior de Investigaciones Científicas, Madrid, Spain*

⁵*Herschel Science Centre, European Space Astronomy Centre, European Space Agency, Postbus 78, E-28691 Villanueva de la Cañada, Madrid, Spain*

⁶*Department of Theoretical Physics, Universidad Autónoma de Madrid, Cantoblanco, E-28049 Madrid, Spain*

⁷*Instituto de Astronomía, Universidad Nacional Autónoma de México, Km. 103 Carr. Tijuana-Ensenada, 22860, Ensenada, B. C., México*

ABSTRACT

We present seeing-limited narrow-band mid-IR GTC/CanariCam images of the spatially extended fullerene-containing planetary nebula (PN) IC 418. The narrow-band images cover the C₆₀ fullerene band at 17.4 μm , the polycyclic aromatic hydrocarbon like (PAH-like) feature at 11.3 μm , the broad 9-13 μm feature, and their adjacent continua at 9.8 and 20.5 μm . We study the relative spatial distribution of these complex species, all detected in the *Spitzer* and *Infrared Space Observatory (ISO)* spectra of IC 418, with the aim of getting observational constraints to the formation process of fullerenes in H-rich circumstellar environments. A similar ring-like extended structure is seen in all narrow-band filters, except in the dust continuum emission at 9.8 μm , which peaks closer to the central star. The continuum-subtracted images display a clear ring-like extended structure for the carrier of the broad 9-13 μm emission, while the spatial distribution of the (PAH-like) 11.3 μm emission is not so well defined. Interestingly, a residual C₆₀ 17.4 μm emission (at about 4- σ from the sky background) is seen when subtracting the dust continuum emission at 20.5 μm . This residual C₆₀ emission, if real, might have several interpretations; the most exciting being perhaps that other fullerene-based species like hydrogenated fullerenes with very low H-content may contribute to the observed 17.4 μm emission. We conclude that higher sensitivity mid-IR images and spatially resolved spectroscopic observations (especially in the Q-band) are necessary to get some clues about fullerene formation in PNe.

Keywords: physical data and processes: astrochemistry — stars: AGB and post-AGB — ISM: molecules — ISM: planetary nebulae: individual (IC 418)

Corresponding author: J. J. Díaz-Luis

jjairo@oan.es, agarcia@iac.es, amt@iac.es, Pedro.Garcia.Lario@esa.int, eva.villaver@uam.es, ggs@astro.unam.mx

1. INTRODUCTION

Spitzer observations have provided the first evidence for the presence of C_{60} and C_{70} fullerenes in Planetary Nebulae (PNe; Cami et al. 2010; García-Hernández et al. 2010, 2011a), reflection nebulae (Sellgren et al. 2010), the two least H-deficient R Coronae Borealis stars (García-Hernández et al. 2011b) and a proto-PN (Zhang & Kwok 2011). In particular, the detection of C_{60} fullerenes together with polycyclic aromatic hydrocarbon like (PAH-like) features in PNe with normal H-abundances indicate that formation of large fullerenes such as C_{60} is favored in the presence of H contrary to theoretical and experimental expectations (García-Hernández et al. 2010). The detection of fullerenes around old stars together with the recent identification of C_{60}^+ as a diffuse interstellar band (DIB) carrier (the only one known to date; Campbell et al. 2015; Walker et al. 2015) indicate that fullerene molecular nanostructures are ubiquitous in the interstellar medium (ISM), and could play a fundamental role in many aspects of circumstellar/interstellar Chemistry and Physics.

The formation process of fullerenes in space is still uncertain and several mechanisms have been proposed in the literature as the most suitable ones: i) the formation in H-poor environments (Goeres & Sedlmayr 1992); ii) high- and low-temperature formation in C-rich environments (Jäger et al. 2009; Fulvio et al. 2017); iii) photochemical processing of hydrogenated amorphous carbon grains (HACs; García-Hernández et al. 2010); and iv) photochemical processing of large PAHs (Berné & Tielens 2012). Hydrogenated species cannot be produced by the first two mechanisms, which is very difficult to reconcile with the astronomical evidence. The two last formation scenarios, involving the photochemical processing of HACs (or similar materials with a mixed aromatic/aliphatic composition; e.g., García-Hernández et al. 2012) and large PAHs, are based on top-down chemical models toward the most stable C_{60} and C_{70} fullerenes.

C_{60} , in the Berné & Tielens (2012) model, is formed top-down from the transformation of large PAHs into graphene under UV radiation from massive stars. Potential problems of the large PAHs scenario above are that: i) yet to date, no specific gas-phase PAH has been identified in space (see e.g., Tielens 2011 for a review); and ii) PAHs cannot explain the origin of the band variations depending on the astrophysical source (e.g., Zhang & Kwok 2015; Álvaro Galué & Díaz Leines 2017). Interestingly, Zhen et al. (2014) reported the first experimental evidence that PAHs with 60 C atoms photoisomerize to C_{60} , while Berné et al. (2015) presented a detailed photochemical modelling for a single PAH

molecule ($C_{66}H_{20}$) that may explain the the top-down formation of fullerenes in the ISM via UV processing of large PAH molecules.

Contrary to the large PAHs fullerene formation scenario, the presence of HAC-like materials in space has been firmly established; e.g., from the detection of the sp^3 CH_3 and CH_2 stretching features contributing to the $3.4 \mu m$ absorption detected in very different astronomical environments (e.g., Alata et al. 2014 and references therein) or the aliphatic discrete emission features (e.g., at 3.4, 3.5, 6.0, 6.9, and $7.3 \mu m$) and broad emission plateaus (e.g., at 6-9 and 9-13 μm) (e.g., Kwok & Zhang 2011 and references therein) associated to HAC-like materials. Fullerenes and PAH-like species in H-containing circumstellar environments may be formed by the decomposition (e.g., by the UV radiation from the central star) of a carbonaceous compound with a mixture of aromatic and aliphatic structures (HAC-like; García-Hernández et al. 2010, 2011a,b, 2012; Micelotta et al. 2012), which should be a major constituent in the circumstellar envelope of C-rich evolved stars. Potential problems to this alternative fullerene formation scenario (the HAC's scenario) are: i) no specific HAC-like particle has been identified in space (e.g., Kwok & Zhang 2011); and ii) the low content of aliphatic C relative to aromatic C apparently estimated from astronomical observations (e.g., Li & Draine 2012). However, the HAC's fullerene formation scenario is suggested by the coexistence of a complex mix of aliphatic and aromatic species such as HACs, PAH clusters, fullerenes, and small dehydrogenated carbon clusters (possibly planar C_{24} or a small fragment of a graphene sheet) in PNe of the Magellanic Clouds and our own Galaxy (García-Hernández et al. 2011a, 2012). The coexistence of these molecular species in PNe with fullerenes is supported by the laboratory experiments carried out by Scott et al. (1997), which showed that the decomposition of HACs is sequential; small dehydrogenated PAH molecules are released first, followed by fullerenes and large PAH clusters. This complex top-down formation process is also supported by the unique spectral variations seen in the IR spectrum of the fullerene-containing RCB star V854 Cen, which indicate that HACs have evolved into complex species such as PAH-like species and fullerene molecules in a timescale of only a decade (García-Hernández et al. 2011b).

In short, both top-down fullerene formation models are quite similar, the main difference being the starting ingredient (HAC-like materials vs. PAHs). Perhaps both models may work in space depending on the astrophysical environment or they could be somekind related; e.g., it could be possible that

HAC- >PAH- >Graphene- >C₆₀ under UV photon irradiation. Interestingly, very recently Álvaro Galué & Díaz Leines (2017) show that the inclusion of nonplanar structural defects in aromatic core molecular structures¹ can explain for the first time the 6–9 μm emission spectral band patterns (i.e., the 6.2, 7.7, and 8.6 μm features usually attributed to PAHs) depending on astrophysical source. They propose that the global regularity of the 6–9 μm IR emission bands is consistent with an emission from the delocalized sp² phase (as π domains) confined in mixed aromatic-aliphatic disordered carbon aggregates (e.g., similar to coal, petroleum fractions, HAC, etc.). The photomechanical processing of HAC-like and PAH-like grains could thus lead to a defective aromatization, being implicated in the top-down formation of fullerenes.

What is the prevalent formation process of fullerenes in circumstellar/interstellar environments? The determination of the relative spatial distribution of fullerenes, PAH-like species, and the yet unidentified 9–13 μm feature carrier may represent the ideal test for answering this question and for understanding the chemistry of large organic molecules in circumstellar/interstellar environments. *Spitzer* observations of fullerene-containing PNe only offer a marginal amount of spatial information at a resolution of 3.6" (spatial information is only possible for low-resolution, R \sim 100, spectroscopy) which does not allow to determine the exact relative spatial distribution of these species. However, seeing-limited Gran Telescopio de Canarias (GTC) observations can improve the spatial resolution by a factor of about 10 with respect to *Spitzer*.

In this paper, we present GTC/CanariCam mid-IR imaging of the extended fullerene-containing PN IC 418. An overview of the observations (and data reduction) and of the dust continuum-subtraction techniques applied to our images are presented in Sections 2 and 3, respectively. In Section 4 we study the relative spatial distribution of the fullerene, PAH-like, and 9–13 μm emissions. Section 5 discusses these results, and the main conclusions of our work are given in Section 6.

2. OBSERVATIONS AND DATA REDUCTION

IC 418 is an elliptical PN, with a major axis of 14 arcsec and a minor axis of 11 arcsec in the optical (Ramos-Larios et al. 2012), which is surrounded by a more extended low-level ionized halo, and, in turn, by a neutral envelope with an angular size of about 2 arcmin (Taylor

& Pottasch 1987; Taylor et al. 1989). This PN displays fullerene and PAH-like (e.g., at 11.3 μm) features, together with a strong and broad 9–13 μm feature (see Fig. 1). Moreover, we selected IC 418 (with an estimated distance of 1.26 kpc; Morisset & Georgiev 2009) for the GTC/CanariCam observations because it is the brightest and most spatially extended source from the known list of Northern fullerene-containing PNe (e.g., García-Hernández et al. 2012; Otsuka et al. 2014).

IC 418 was observed at the GTC with the mid-infrared camera CanariCam (Telesco et al. 2003) in service mode in January and December 2013. CanariCam can perform mid-infrared (7.5–25 μm) imaging using a set of narrow, medium and broad-band filters. The seeing, in the V band, during the observations was 0.9" and 1.7" for the N (10 μm) and Q (20 μm) images, respectively. This corresponds to a FWHM of 0".66 and 1".2 for the N and Q bands, respectively. Therefore the images are seeing limited. These mid-IR images were obtained by using narrow-band filters centered around the position of the features of our interest: PAH-like at 11.3 μm (PAH2, $\Delta\lambda = 0.6 \mu\text{m}$), 9–13 μm at 11.75 μm (SiC, $\Delta\lambda = 2.5 \mu\text{m}$), and C₆₀ at 17.65 μm (Q1, $\Delta\lambda = 0.9 \mu\text{m}$), as well as their adjacent continua at 9.8 μm (Si3, $\Delta\lambda = 1.0 \mu\text{m}$), and 20.5 μm (Q4, $\Delta\lambda = 1.0 \mu\text{m}$).

In order to map the inner regions (<20"), we have used the off-chip chopping and nodding techniques, that consist of introducing small offsets in multiple images to remove most of the background emission, the thermal emission from the telescope, and the detector noise. Moreover, the off-chip mode means that the negative images (from the off-source chop beam) are not seen in the detector image. The chop and nod position angles were 75° and –105°, respectively, with throws of 40 arcsec. We got one final summed image of IC 418 in the Si3, PAH2, and SiC filters, while we averaged 2 and 3 summed images in the Q1 and Q4 filters, respectively, in order to get a final image for each Q-band filter.

Because we did not observe standard stars for flux calibration on the same nights as PN IC 418, we have followed two different procedures for flux calibration: i) using the observations of standard stars (HD 70272 and HD197989; available from the GTC data archive) that were observed at observational conditions as similar as possible to those of IC 418 but on different dates; and ii) using the *Infrared Space Observatory (ISO)* spectrum that covers the full nebula and assuming no significant IC 418 IR spectral variability in the last \sim 30 years (see below). In the first case, the final images were processed using the pipeline RedCan (González-Martín et al. 2013), which produces final flux-calibrated (in Jy) images from the GTC/CanariCam raw data. Since the

¹ Note that defective out-of plane aromatic-like structures are 3D species, not falling under the standard (2D) PAHs chemical definition (see Álvaro Galué & Díaz Leines 2017).

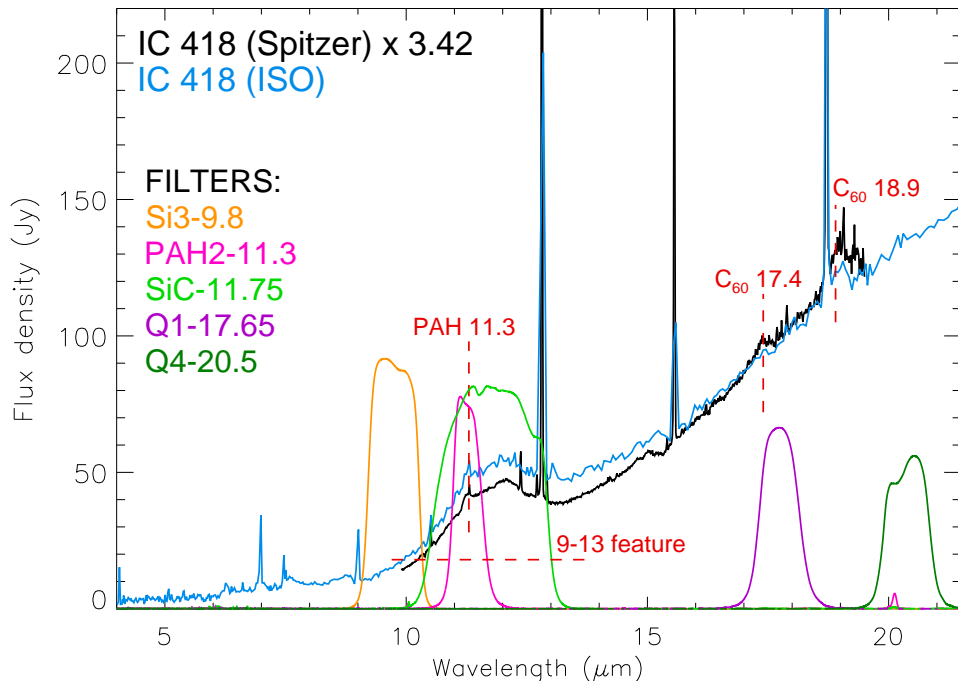


Figure 1. *ISO* (in blue) and *Spitzer* (in black) IR spectra of the PN IC 418 plotted together with the profiles of the five CanariCam filters used in the observations. The positions of the C_{60} bands at 17.4 and 18.9 μm , and the PAH-like feature at 11.3 μm (red dashed vertical lines) are marked. The broad 9–13 μm feature (red dashed horizontal line) is also marked.

observations of the standard stars were made on different dates, in principle, the flux calibration may be quite uncertain; although we get $\sim 10\text{--}30\%$ (depending on the filter) relative flux differences between GTC/CanariCam and *ISO*. In the second case, we first calculated the synthetic photometry (in Jy) through all CanariCam filters from the *ISO* spectrum using the SMART² software and we then calibrated our mid-IR images in order to get a total summed flux (in Jy) that coincides with the synthetic photometry. In Figure 2, we show the *ISO* spectrum of IC 418 in comparison to the observed WISE (Cutri et al. 2013), AKARI (Ishihara et al. 2010), and IRAS (Helou & Walker 1988) photometry, as well as the corresponding synthetic photometry (again obtained from the *ISO* spectrum using SMART) in each one of the WISE, AKARI, and IRAS filters. There is no significant flux variation in the last ~ 30 years; the only exception is the WISE W4 flux density, which seems to deviate from the *ISO* spectrum likely due to known saturation issues. Table 1 gives the filter names, total on-source exposure times, signal-to-noise ratio (S/N), observational

dates, integrated fluxes, synthetic photometry, and the PN size in each mid-IR filter as derived from our images.

Figures 3 and 4 show the final flux-calibrated mid-IR GTC/CanariCam images of IC 418 using the synthetic photometry (case ii above). The PAH2 and SiC filters (with different widths) cover the PAH-like feature at 11.3 μm , the broad 9–13 μm feature, and dust continuum emission, while the Q1 filter covers the C_{60} emission band at 17.4 μm and dust continuum emission. The Si3 and Q4 filters cover the dust continuum emission at 9.8 and 20.5 μm , respectively (see Fig. 1). In short, a similar ring-like extended structure is seen in all GTC/CanariCam filters, with the exception of the Si3 filter that shows that the dust continuum emission at 9.8 μm peaks closer to the central star. Note that we can exclude any significant contribution from the intense emission line of Ne II at 12.81 μm to the SiC filter, as this line has only a contribution of $\sim 8.2\%$ to the synthetic photometry in that filter. Moreover, the similar distribution of the PAH2 and SiC images suggests that we are seeing the emission, but may not be contributing too much.

Finally, narrow-band Hubble Space Telescope (HST) WFPC2 images of IC 418 in the [N II] $\lambda 6583$ and [O III] $\lambda 5007$ emission lines were retrieved from the Mikulski Archive for Space Telescopes (MAST; Prop. ID: 8773) for comparison with our mid-IR images.

² The Spectroscopic Modeling Analysis and Reduction Tool (SMART), is a software package to reduce and analyze data from the Infrared Spectrograph (IRS) on the *Spitzer Space Telescope*. Cornell maintains information on their website for SMART and updates it regularly. See <http://isc.astro.cornell.edu/smart>.

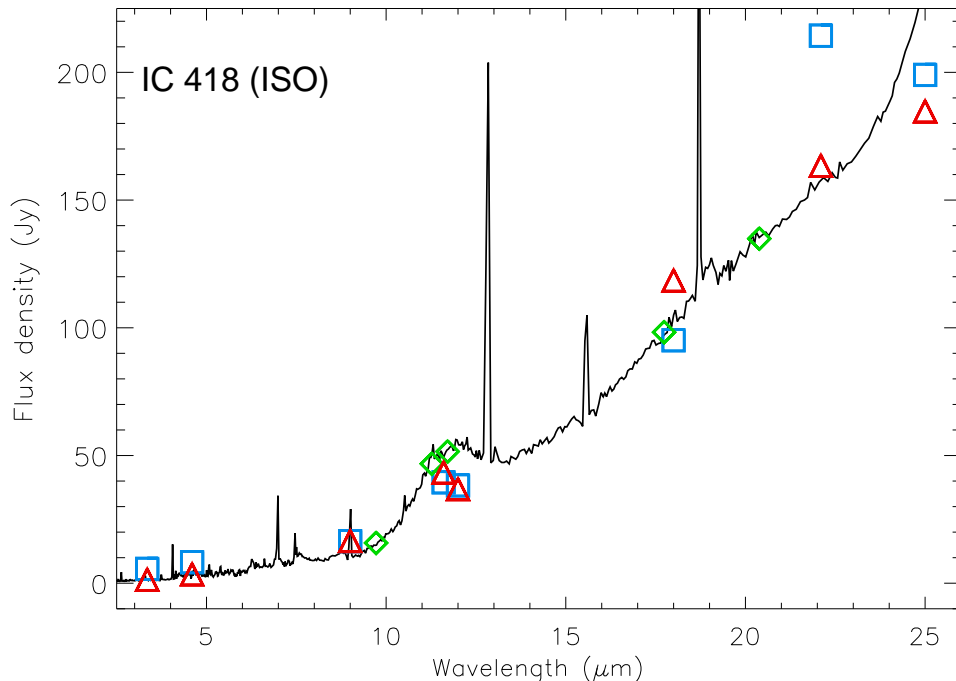


Figure 2. *ISO* spectrum of the PN IC 418 in comparison to observed (squares) and synthetic (triangles) *AKARI*, *WISE*, and *IRAS* photometry. The GTC/CanariCam (diamonds) synthetic photometry is also displayed for comparison.

The 200-s [O III] image was obtained from one individual exposure acquired through the F502N filter (central wavelength $\lambda_c = 5012 \text{ \AA}$ and bandwidth $\Delta\lambda = 27 \text{ \AA}$), whereas the 300-s [N II] image was obtained from one individual exposure acquired using the F658N filter ($\lambda_c = 6591 \text{ \AA}$, $\Delta\lambda = 29 \text{ \AA}$). Cosmic rays were removed using the *Lacos_im* package of van Dokkum (2001).

3. DUST CONTINUUM-SUBTRACTION

In order to study the relative spatial distribution of C_{60} fullerenes, PAH-like molecules, and the 9-13 μm feature carrier, we have subtracted the dust continuum contribution by using the Si3 (9.8 μm) and Q4 (20.5 μm) images.

The continuum subtraction from our images is complicated because the central star of PN IC 418 (nor any field star) is not detected in our mid-IR images. Since our flux-calibrated images and the *Spitzer* and *ISO* spectra of IC 418 are in the same flux units (Jy), we have then only taken into account the slope of these spectra; i.e., the relative differences between the measured fluxes in the continuum at the central wavelength in all filters are used to scale the continuum images and subtract the dust continuum contribution³. In order to estimate the dust continuum contribution for each filter, we have fitted a polynomial spline of order 4 to the continuum

(free from any gas/dust feature) in the *Spitzer* and *ISO* spectra by using standard tasks in IRAF⁴ (see Fig. 5).

By assuming that the continuum flux ratios (or relative differences) between the wavelengths of our interest are similar in both *Spitzer/ISO* spectra and GTC/CanariCam images (see above about the non IR variability of IC 418 during the last ~ 30 years; Fig. 2), we find that we have to scale the Q4 image by a factor of ~ 0.70 for the case of the Q1–Q4 continuum-subtraction. The Si3 images have to be scaled by factors of ~ 1.90 and 2.17 for the PAH2–Si3 and SiC–Si3 continuum-subtractions, respectively. Moreover, in order to extract the PAH-like 11.3 μm emission from the PAH2 image (PAH2–SiC), we have to scale the SiC image (assumed to be dominated by the broad 9-13 μm emission; see Fig. 1) by a factor of ~ 0.87 . The final continuum-subtracted images have been boxcar smoothed with a 2x2 window. Figures 6 and 7 show the resulting PAH2–Si3, SiC–Si3, and Q1–Q4 continuum-subtracted images as well as the PAH2–SiC subtracted image, which were flux-calibrated using the synthetic photometry (case ii) and the standard stars (case i), respectively.

⁴ Image Reduction and Analysis Facility (IRAF) software is distributed by the National Optical Astronomy Observatories, which are operated by the Association of Universities for Research in Astronomy, Inc., under cooperative agreement with the National Science Foundation.

³ The relative flux differences are very similar in the *Spitzer* and *ISO* spectra (see Fig. 1).

Table 1. Summary of observational data

Filter ^a	λ_c (μm)	Time ^b (s)	S/N ^c	Date	Flux ^d (Jy)	SP ^e (Jy)	Size ^f
Si3 (cont ^g)	9.8	661	13	2013 Jan 20	4.52	15.76	13.6" x 15.5"
PAH2 (PAH-like + 9-13 μm + cont ^g)	11.3	626	15	2013 Jan 20	36.76	46.78	14.3" x 17.4"
SiC (PAH-like + 9-13 μm + cont ^g)	11.75	413	13	2013 Jan 2	42.39	51.56	13.8" x 16.0"
Q1 (C ₆₀ + cont ^g)	17.65	1274	10	2013 Dec 29	93.93	98.28	14.2" x 16.0"
Q4 (cont ^g)	20.5	1911	12	2013 Dec 29-30	112.69	134.91	14.6" x 17.1"

^aThese are the names given to each CanariCam filter.

^bTotal on-source exposure time.

^cS/N is an average of several measurements in each image.

^dIntegrated fluxes when calibrating with the standard stars HD 70272 and HD197989 (see text for more details). The fluxes were measured defining the PN size in each mid-IR filter at the 3σ level (from the mean sky background) using the Graphical Astronomy and Image Analysis Tool (GAIA; <http://star-www.dur.ac.uk/~pdraper/gaia/gaia.html>). Flux errors are estimated to be in the range 10-30% (depending on the filter).

^eSynthetic photometry through all CanariCam filters from the *ISO* spectrum using SMART (see text for details).

^fSizes measured at the 3σ level (from the mean sky background) in each mid-IR filter with standard tasks in IRAF.

^gDust continuum emission.

The continuum-subtracted images obtained using the standard stars for flux calibration (case i; Fig. 7) seem to be of poorer quality than those obtained using the synthetic photometry (case ii; Fig. 6). This is due to the use of standard stars observed on different dates (at slightly different weather conditions), which produces non-systematic flux uncertainties that vary randomly among the GTC/CanariCam filters; the relative flux differences between GTC/CanariCam and *ISO* vary between ~ 10 and 30% (depending on the filter; see Table 1). This is clearly evidenced by the resulting PAH2–Si3 and SiC–Si3 images (case i; Fig. 7) that show a strong excess emission closer to the central star. This excess of emission in the inner regions of the nebula is an artifact due to a bad removal of the dust continuum emission at $9.8 \mu\text{m}$ (Si3 filter; see Fig. 3). The resulting PAH2–Si3 and SiC–Si3 images obtained with the case ii) flux calibration (Fig. 6) do not display such excess emission, indicating that the Si3 dust continuum contribution is subtracted correctly. Taking into account this and the non-IR variability of IC 418 (Fig. 2) in the following we thus make use of the continuum-subtracted images obtained using the synthetic photometry (case ii) flux calibration).

4. RESULTS

4.1. Fullerene emission

The Q1 and Q4 images (see Fig. 3) show a similar ring-like structure, which indicates that fullerenes may be co-spatial with the dust continuum emission (e.g., they could be attached to the dust grains) or that both images are dominated by the dust continuum emission. IC 418 displays a very low C₆₀-to-continuum ratio (e.g., $F_{17.4}/F_{cont} \sim 0.06$, see below) and the similar spatial distribution seen in the Q1 and Q4 images already suggests that both images are likely dominated by the strong dust continuum emission. The continuum-subtracted fullerene emission (the Q1–Q4 image in Fig. 6) is very weak (at $\sim 4\sigma$ from the mean background level) and mainly located at the northeast, extending from the inner (even near the central star) to the outer regions of the nebula. Due to the low C₆₀-to-continuum ratio we cannot discard additional weaker fullerene emission from rest of the ring-like structure seen in the Q1 image. Indeed, changing by ~ 5 -20% the factor used to subtract the Q4 continuum contribution, one can recover the ring-like structure in the resulting Q1–Q4 image. Alternatively, the emission may originate in an ellipsoid around the central star and we see such distribution due to projection effects (see e.g., Machado 2004).

We note that the *Spitzer*/IRS SH slit only covers part of the nebula, while the ISO SWS diaphragm covers the entire nebula (see Pottasch et al. 2004 and Otsuka et al. 2014 for more details). In Figure 6, we display the

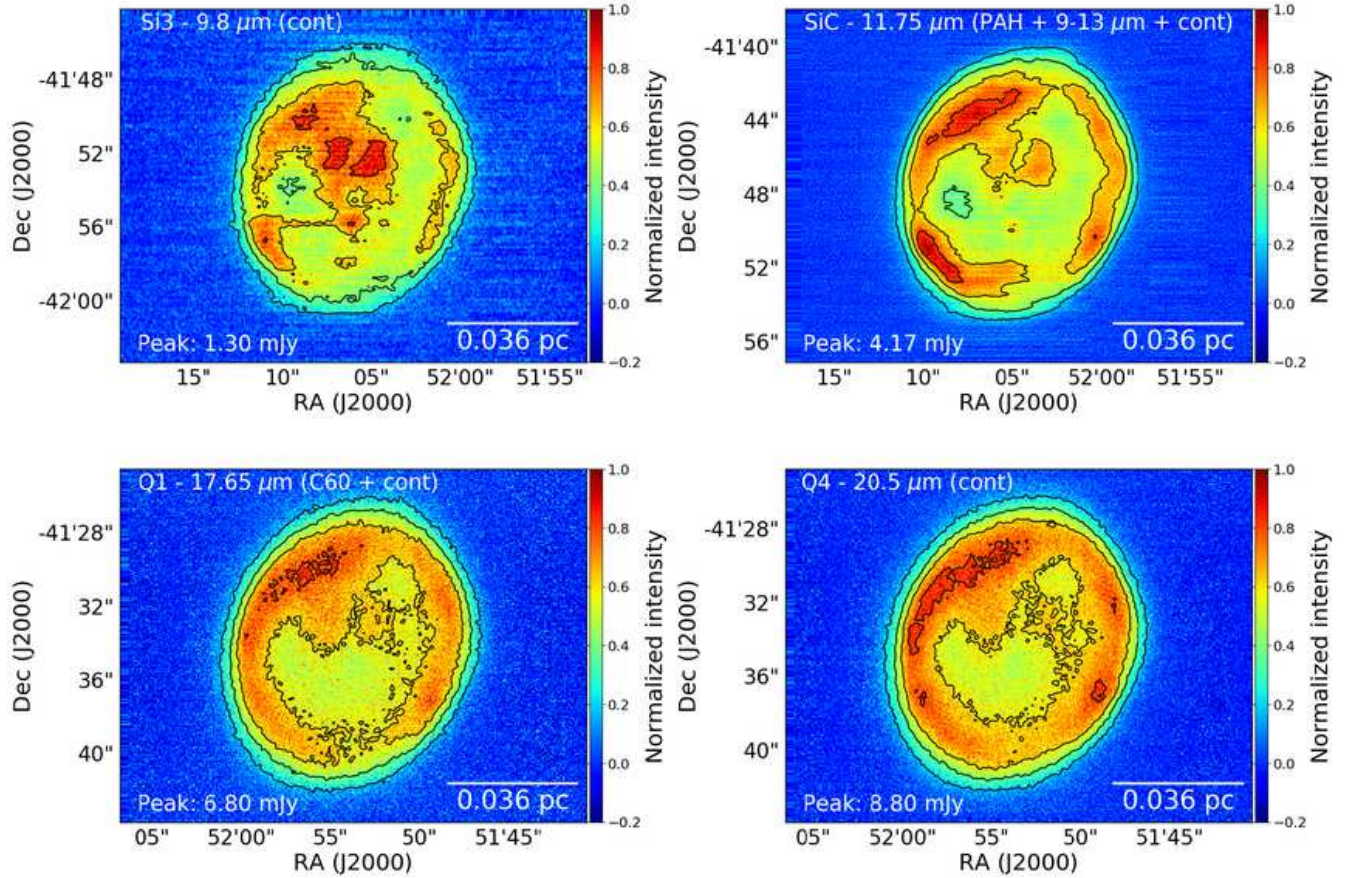


Figure 3. Contour maps of the flux-calibrated mid-IR GTC/CanariCam images of the C₆₀-PN IC 418 in the Si3 (continuum at 9.8 μm), SiC (PAH-like + 9-13 μm + continuum at 11.75 μm), Q1 (C₆₀ + continuum at 17.65 μm), and Q4 (continuum at 20.5 μm) filters. All contour maps have been normalized to the peak flux in the image. North is up, east is left. The bar in the lower right corner illustrates 0.036 pc at the estimated distance to IC 418 (1.26 kpc; Morisset & Georgiev 2009). Contours range from 0.2 to 0.8 with 3 steps of 0.2 each.

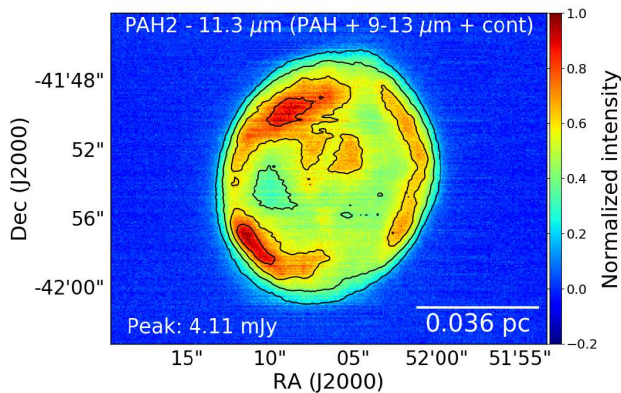


Figure 4. Contour map of the flux-calibrated mid-IR GTC/CanariCam image of the C₆₀-PN IC 418 in the PAH2 (PAH-like + 9-13 μm + continuum at 11.3 μm) filter. The notation is the same as in Figure 3.

with the *Spitzer*/IRS SH slit. Interestingly, the *Spitzer* slit just covers the northeast region of the nebula, where the residual fullerene emission seems to be located. This could explain why *Spitzer* clearly detected the fullerene IR features in IC 418 and it would suggest that the residual fullerene emission observed could be real. We have measured the integrated fluxes of the C₆₀ bands at 17.4 and 18.9 μm (with SMART) in the *Spitzer* and *ISO* spectra (see Fig. 5). In Table 2, we list the central wavelengths and integrated fluxes for these two C₆₀ fullerene bands in both *Spitzer* and *ISO* spectra. The integrated fluxes of both C₆₀ bands in the *ISO* spectrum are four times higher than those of the *Spitzer* one, as expected because of the larger *ISO* aperture and the fact that weaker fullerene emission could be uniformly distributed along the nebula (Figs. 6 and 7). We measure C₆₀ F(17.4)/F(18.9) flux ratios of 0.50 ± 0.12 and 0.39 ± 0.24

Q1–Q4 continuum-subtracted image of IC 418 overlaid

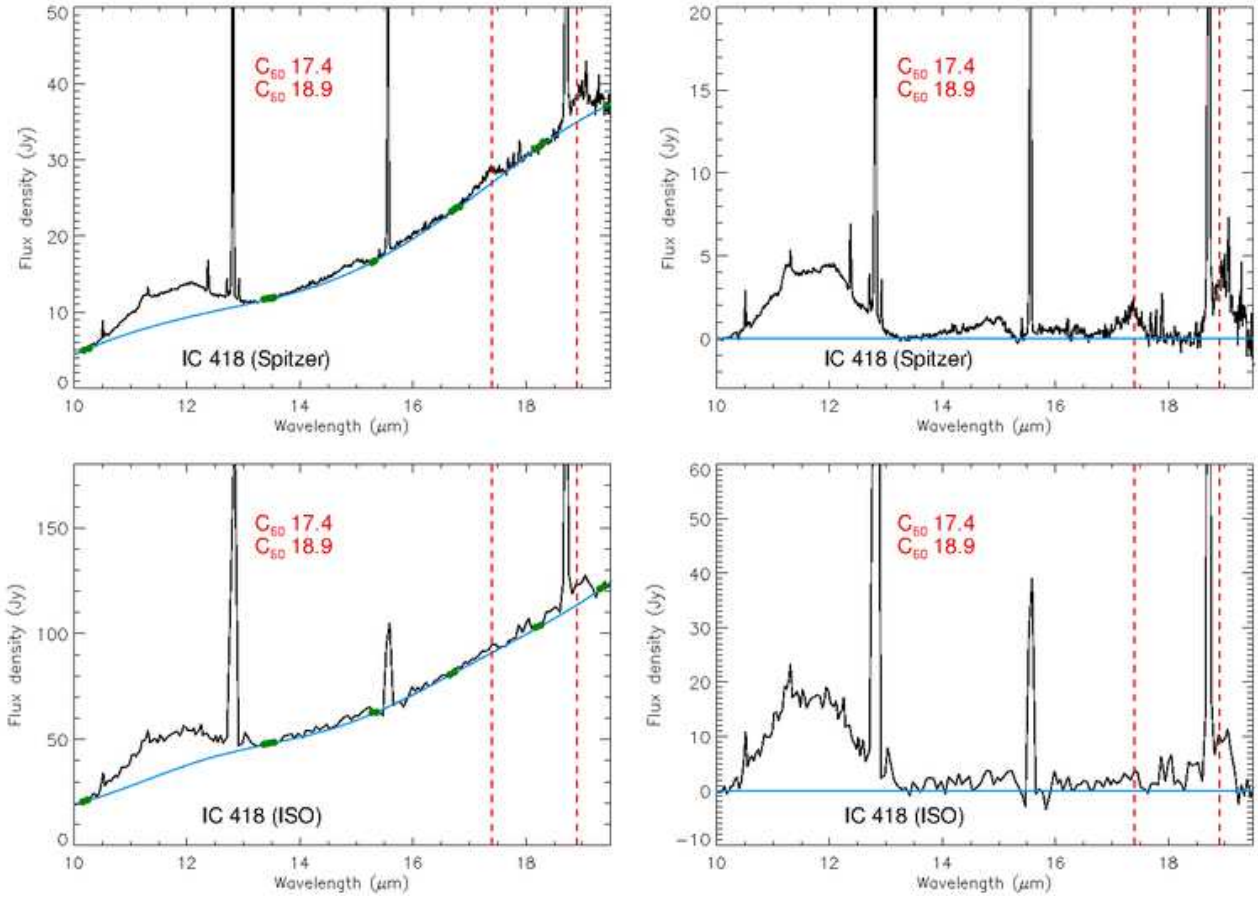


Figure 5. Polynomial fits made to the dust continuum of the *Spitzer*/IRS and *ISO* spectra (left panels) and the corresponding residual spectra (right panels) for the fullerene PN IC 418. Both left panels display the observed IR spectra (in black) together with a polynomial fit (in blue) to continuum points free from any gas and dust feature (in green). The corresponding residual or dust continuum subtracted spectra (in black) are shown in right panels. The band positions of the C_{60} features at 17.4 and 18.9 μm (red dashed vertical lines) are indicated.

in the *Spitzer* and *ISO* spectra, respectively⁵; both ratios are similar within the errors. The feature-to-continuum ratios of the C_{60} 17.4 and 18.9 μm bands, however, are slightly higher in the *Spitzer* spectrum (0.063 ± 0.004 and 0.113 ± 0.007 , respectively) than in the *ISO* (0.037 ± 0.008 and 0.089 ± 0.009 , respectively) spectrum, which again might indicate that the excess of fullerene 17.4 μm emission is real. Indeed, the integrated fluxes measured in the Q1–Q4 and SiC–Si3 images, along the *Spitzer* SH slit, are $\sim 2.09 \times 10^{-18}$ and $3.07 \times 10^{-17} \text{ Wcm}^{-2}$, which are ~ 3.5 and 1.2 times higher than the C_{60} 17.4 μm and 9–13 μm integrated fluxes measured in the *Spitzer* spectrum (Table 2). Otherwise, we cannot discard the

⁵ We note that Otsuka et al. (2014) measured a C_{60} $F(17.4)/F(18.9)$ flux ratio of 0.46 ± 0.03 in the IC 418 *Spitzer* spectrum, which agrees well, within the errors, with the one derived here.

Table 2. Mid-IR C_{60} features in the PN IC 418^a

<i>Spitzer</i> spectrum		<i>ISO</i> spectrum	
λ (μm)	Flux (Wcm^{-2})	λ (μm)	Flux (Wcm^{-2})
17.35	$6.05\text{e-}19(\pm 0.72)$	17.32	$1.31\text{e-}18(\pm 0.52)$
18.97	$1.20\text{e-}18(\pm 0.15)$	18.97	$3.35\text{e-}18(\pm 0.75)$

^a Estimated flux errors (between brackets) are always less than $\sim 30\%$ - 40% (estimated by SMART).

possibility that the intensity of fullerene emission at 17.4 μm has varied spatially.

The synthetic photometry through the GTC/Canari-Cam filters PAH2, SiC, and Q1 from the *Spitzer* spectrum gives values of 11.42, 13.17, and 29.55 Jy, respec-

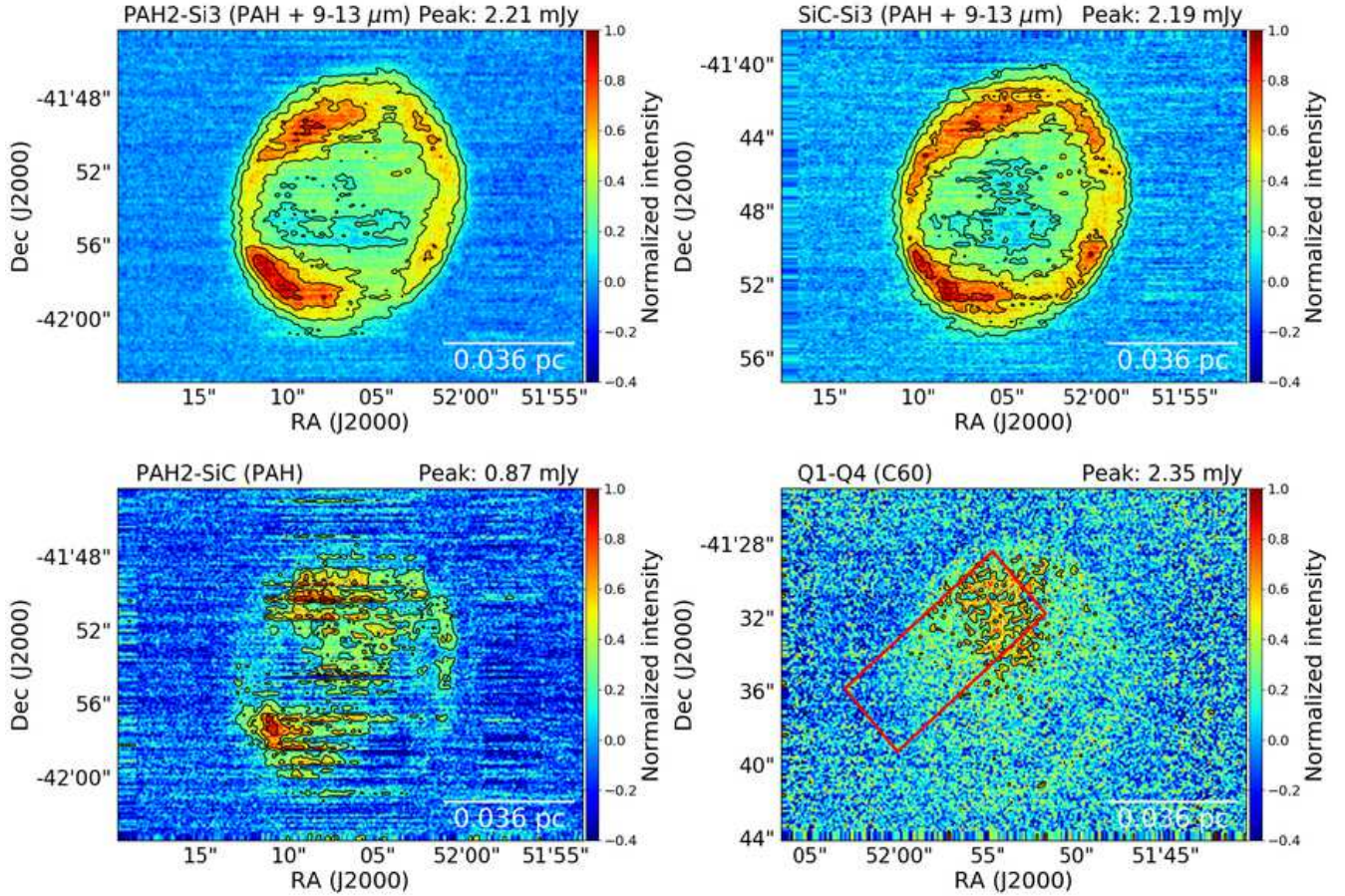


Figure 6. Contour maps of the mid-IR GTC/CanariCam PAH2–Si3, SiC–Si3, PAH2–SiC, and Q1–Q4 images of IC 418. The flux calibration was performed using the synthetic photometry (case ii in the text) and all contour maps have been normalized to the peak flux in the image. In the PAH2–Si3, SiC–Si3, and PAH2–SiC images, contours range from 0.2 to 0.8 with 3 steps of 0.2 each. In the Q1–Q4 image only one contour at 0.4 is displayed. Note that the position and the size of *Spitzer*/IRS SH slit is indicated by the red box (dimension: 4.7" x 11.3") superimposed to the Q1–Q4 image.

tively, while by summing the flux in our GTC/CanariCam images, in these three filters along the *Spitzer* aperture (see Fig. 6), we get integrated fluxes of 15.90, 17.56, and 31.61 Jy, respectively. The fluxes measured in our GTC/CanariCam images in the filters covering the C₆₀ 17.4 μm (Q1) and the broad 9–13 μm (SiC) emissions are thus about 7% and 25% higher than those from the *Spitzer* spectrum; 28% higher for the narrower PAH2 filter.

Even if the flux calibration errors in our GTC/CanariCam data are difficult to estimate, this also suggests a 17.4 μm excess emission in our GTC/CanariCam observations compared with the *ISO* ones, which is in line with the apparent 17.4 μm excess emission in the *Spitzer* spectrum.

Finally, it is to be noted here that we have assumed that the 17.4 μm flux observed in IC 418 is mostly due to C₆₀ fullerenes, being not contaminated by PAH-like 17.4 μm emission. This is because PAH-like features

in C₆₀-PNe are very weak (see e.g., García-Hernández et al. 2012; Otsuka et al. 2014), unlike the case of RNe and RCB stars whose mid-IR spectra are PAH-like dominated. The PAH-like 17.4 μm band is correlated with the PAH-like 16.4 μm band (Berné & Tielens 2012) and the latter is only present in RNe and RCBs (with PAH-like dominated spectra), being completely absent in all C₆₀-PNe with different degrees of PAH-like emission; from almost no PAH-like (e.g., Tc 1) to relatively stronger PAH-like emission (e.g., K 3-62). Among C₆₀-PNe, the normalized line profiles of the 17.4 and 18.9 μm C₆₀ bands are very similar and the F(17.4 μm)/F(18.9 μm) ratio remains almost constant (e.g., Otsuka et al. 2014). This already suggests that possible PAH-like 17.4 μm is very likely a minor contribution to the observed 17.4 μm flux. On the other hand, with a slight extrapolation of Boersma et al. (2010)'s Figure 5 (showing a correlation between the 6.2/11.3 μm and 16.4/11.3 μm PAH-like flux ratios), the 16.4 μm band

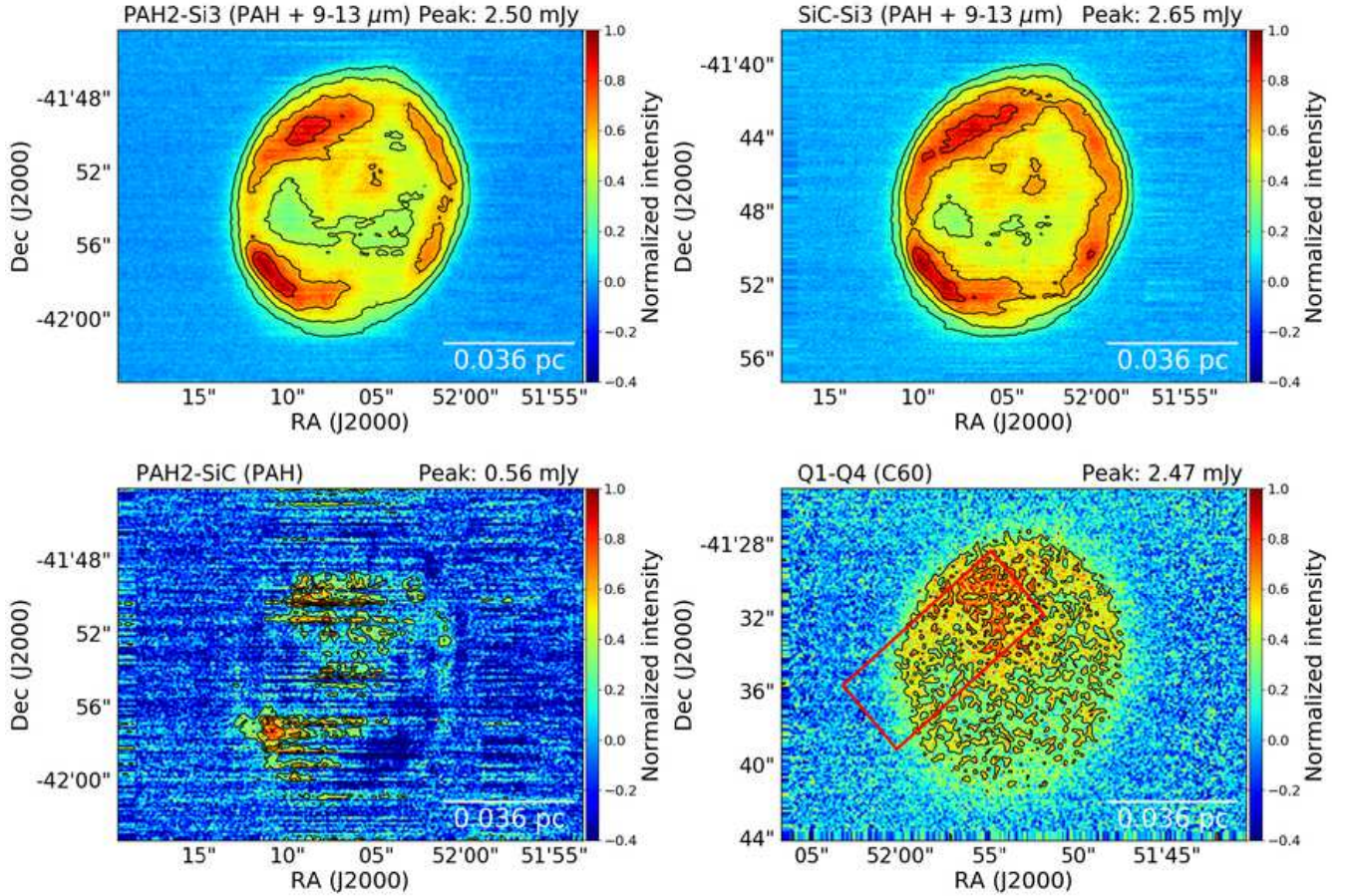


Figure 7. Contour maps of the mid-IR GTC/CanariCam PAH2–Si3, SiC–Si3, PAH2–SiC, and Q1–Q4 images of IC 418 when calibrating with the standard stars (case i in the text). The notation is the same as in Figure 6 but the contours are slightly different. In particular, only two contours at 0.4 and 0.6 are displayed in the Q1–Q4 image.

is predicted to have an intensity $\sim 5\%$ that of IC 418’s $11.3\mu\text{m}$ band (i.e., $F(16.4\mu) \sim 1.37 \times 10^{-15} \text{ Wm}^{-2}$), which is consistent with the feature’s absence (i.e., well below our estimated upper limits). Other PAH-like features in this spectral region are thus expected to be weaker. For example, in the outer regions of the RNe NGC 7023, the $17.4\mu\text{m}$ band is 100% due to PAH-like species and $F(17.4\mu)/F(16.4\mu) = 0.35$ (Berné & Tielens 2012), while the latter ratio is typically ~ 0.05 in no C₆₀-PNe (e.g., Boersma et al. 2010). In the range $F(17.4\mu)/F(16.4\mu) \sim 0.35 - 0.05$, the expected PAH-like $17.4\mu\text{m}$ contribution to the $17.4\mu\text{m}$ flux observed in IC 418, would be $\sim 27 - 191$ times lower. Thus, assuming that the shape of the spectrum remains constant over the nebula (this is at least true for the ISO and Spitzer spectra), we conclude that the observed $17.4\mu\text{m}$ is very likely uncontaminated by PAH-like blends.

4.2. $11.3\mu\text{m}$ PAH-like + $9-13\mu\text{m}$ carrier emission

The Si3 image displays the strongest emission near the IC 418 central star and weaker emission (mainly at the

northeast and southeast of the nebula) from the outer ring-like structure. The PAH2 and SiC images, however, show the strongest emission from the outer ring-like structure with the weaker emission near the central star, where the Si3 emission is maximum (see Figs. 3 and 4). The $11.3\mu\text{m}$ PAH-like + $9-13\mu\text{m}$ carrier emission is obtained by doing the PAH2–Si3 and SiC–Si3 subtractions (see Fig. 6). The PAH2–Si3 and SiC–Si3 continuum-subtracted images display an identical spatial distribution. The similar morphology together with the very weak PAH-like $11.3\mu\text{m}$ feature (see Fig. 1) suggest that the emission is dominated by the $9-13\mu\text{m}$ carrier in both filters. The latter is confirmed by the PAH2–SiC subtraction (see below). The $9-13\mu\text{m}$ carrier emission is distributed around the outer ring-like structure, with the strongest emission (at more than 13σ from the mean background level in Fig. 6) at the northeast (and southeast) sides of the nebula.

The spatial distribution of the $9-13\mu\text{m}$ carrier emission is very similar to the dust continuum emission at $20.5\mu\text{m}$ (Q4), which suggests that the $9-13\mu\text{m}$ car-

rier is co-spatial with the dust grains emitting at $20.5 \mu\text{m}$. On the other hand, by comparing the Si3 and SiC images with the IC 418 Hubble Space Telescope images in several optical nebular emission lines (see Fig. 8), we find that the dust continuum emission at $9.8 \mu\text{m}$ is very similar to the [O III] nebular emission at 502 nm , indicating that dust grains coexist with ionized material. We also find that the $9\text{--}13 \mu\text{m}$ carrier + $11.3 \mu\text{m}$ PAH-like emission is somehow similar to the [N II] nebular emission at 658 nm , indicating that these molecules may coexist with ionized material in the outer regions of the nebula.

Interestingly, we could separate the PAH-like emission at $11.3 \mu\text{m}$ from the PAH2 image by doing the PAH2–SiC subtraction (see Fig. 6). The PAH2–SiC image displays a less extended residual emission with intensity peaks (at $\sim 5\sigma$ from the mean background level in Fig. 6) at the northeast and southeast sides of the nebula. This suggests that the ring-like structure seen in the PAH2–Si3 and SiC–Si3 continuum-subtracted images is mostly due to the $9\text{--}13 \mu\text{m}$ carrier emission and that the aromatic-like component coexist with the $9\text{--}13 \mu\text{m}$ carrier.

4.3. Intensity profiles

Normalized intensity profiles through the individual images (Si3, PAH2, SiC, Q1, and Q4 filters) and subtracted images (PAH2–Si3, SiC–Si3, PAH2–SiC, and Q1–Q4) at position angles (P.A.) of 70° and 110° from east in a clockwise direction are shown in Fig. 9. These P.A. were selected to trace the residual fullerene emission (P.A. = 70°) as well as the ring-like structure along the major nebular axis (P.A. = 110°). The profiles are made by doing a cross-cut through the x-axis and a block average of 50 lines through the y-axis. We have chosen an arbitrary number of lines that corresponds to 4 arc-sec.

The intensity profiles along the Q1 and Q4 images have the same shape (independently of the P.A.) because the continuum contribution is likely dominating the emission in both filters, while the intensity profile along the Q1–Q4 show the location and extension of the residual fullerene emission (upper panels in Fig. 9). The same behaviour is seen for the PAH2 and SiC filters and their intensity profiles are very similar (they mainly trace the outer ring-like structure) because both filters just cover the same features but with different filter width. However, both PAH2 and SiC intensity profiles are different to the Si3 intensity profile (covering the continuum at $9.8 \mu\text{m}$), which shows the maximum intensities at $\sim 1.2''$ from the central star ($\sim 1512 \text{ AU}$ at 1.26 kpc ; Morisset & Georgiev 2009; see Fig. 9). It is no-

table that the outer ring-like structure is clearly seen in the SiC–Si3 and PAH2–Si3 profiles, where the continuum contribution has been greatly subtracted from the SiC and PAH2 profiles. Finally, the PAH2–SiC profiles show the residual excess emission towards the northeast of the nebula (P.A. = 70°) as well as the even weaker (and more homogenous) emission along the major nebular axis (P.A. = 110°).

The residual fullerene emission (see Fig. 9) mainly extends (almost uniformly) from the central star to $\sim 7''$ at the northeast side of the nebula ($\sim 8820 \text{ AU}$), peaking at $\sim 4.5\text{--}5.5''$ ($\sim 5670\text{--}6930 \text{ AU}$); a secondary much weaker (and tentative) peak is also present at the opposite side of the nebula at $\sim 5.5\text{--}6''$ ($\sim 6930\text{--}7560 \text{ AU}$). The $9\text{--}13 \mu\text{m}$ carrier (+ weak $11.3 \mu\text{m}$ PAH-like) emission is distributed along the ring-like structure with emission peaks at similar distances from the central star position (at $\sim 4.5''$ and $\sim 5.5''$ at the northeast and southwest sides of the nebula) with extremely weak emission in the inner regions. The weak $11.3 \mu\text{m}$ PAH-like emission, on the contrary, seems to be located in a more internal region than the $9\text{--}13 \mu\text{m}$ carrier, peaking at $\sim 4''$ ($\sim 5040 \text{ AU}$) at the northeast side of the nebula (see the bottom-left panel in Fig. 9); another peak emission of similar strength (which is not traced by the intensity profiles at P.A. = 110° displayed in the bottom-right panel in Fig. 9) is seen at a similar distance towards the southeast.

5. DISCUSSION

The obtained mid-IR images provide information about the spatial distribution of the fullerene and PAH-like features as well as of the $9\text{--}13 \mu\text{m}$ feature carrier in a fullerene-rich PN such as IC 418.

Fullerene emission at $17.4 \mu\text{m}$ extends from the central star to $\sim 8820 \text{ AU}$ at the northeast side of the nebula (the maximum intensity is at $\sim 6300 \text{ AU}$). This is comparable to the case of the other known fullerene-rich extended PN Tc 1, where lower spatial resolution *Spitzer* observations suggest that the $8.5 \mu\text{m}$ fullerene emission peaks at $6400\text{--}9700 \text{ AU}$ from the central star (Bernard-Salas et al. 2012)⁶. Furthermore, Bernard-Salas et al. (2012) found that fullerene emission at $8.5 \mu\text{m}$ and PAH-like emission at $11.3 \mu\text{m}$ seem to be displaced from the central star and peak at opposite directions, while the IR emission at $9 \mu\text{m}$ (dust continuum) and $12 \mu\text{m}$ (the $9\text{--}13 \mu\text{m}$ carrier) are less extended and centered on the Tc 1's central star. In the case of PN IC 418, however, it seems that

⁶ A complete ring-like structure of the C_{60} $8.5\mu\text{m}$ emission, at a similar distance of $\sim 8000 \text{ AU}$, seems to be confirmed by preliminary (non-continuum subtracted) higher spatial resolution images of Tc 1 from Gemini-S/Treces (Golriz et al., in prep.).

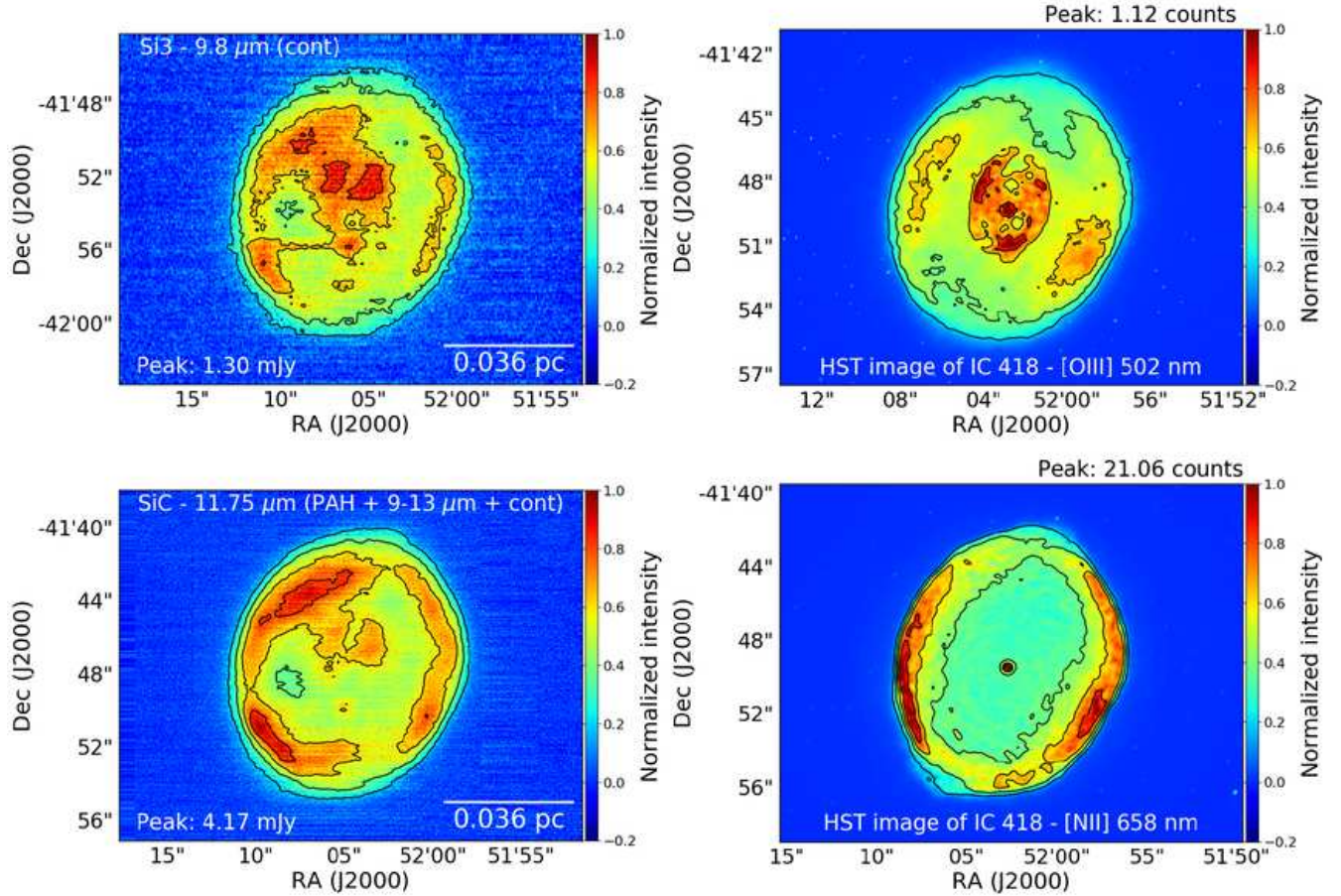


Figure 8. Contour maps of the C_{60} -PN IC 418 in the mid-IR GTC/CanariCam filters at 9.8 and 11.75 μm (left panels) and the optical HST F502N and F658N filters at 502 and 658 nm (right panels), respectively. All contour maps have been normalized to the peak flux in the image and contours range from 0.2 to 0.8 with 3 steps of 0.2 each. North is up, east is left. Note the similarity between the continuum emission at 9.8 μm and [O III] nebular emission at 502 nm, and also between the emission at 11.75 μm (9-13 μm carrier + 11.3 μm PAH-like emission + continuum) and [N II] nebular emission at 658 nm.

fullerene 17.4 μm and PAH-like 11.3 μm are not necessarily co-spatial but both emissions have peaks towards the northeast of the nebula; although at slightly different distances from the central star (at ~ 6300 and ~ 5040 AU, respectively). However, the emission may originate in an ellipsoid around the central star and we see such distribution due to projection effects (see e.g., Manchado 2004). In IC 418, the dust continuum emission at 9.8 μm is also extended and peaking near the central star (at ~ 1512 AU), but the 9-13 μm carrier is mainly distributed in the outer ring-like structure. Thus, it is not actually clear if the 12 μm emission in Tc 1 might be dominated by the dust continuum or by the 9-13 μm carrier. In our mid-IR images of IC 418, it seems clear that the 9-13 μm carrier emission dominates over the adjacent dust continuum emission.

The interpretation of our IC 418 GTC/CanariCam mid-IR images regarding the dominant fullerene formation process in PNe is somewhat contradictory (not con-

clusive). The presence of fullerene emission near the central star, where the 9-13 μm emission is much weaker, would suggest that C_{60} may be a photo-product of the 9-13 μm carrier. This would agree with the idea of fullerenes being formed from the photochemical processing of HAC-like materials (e.g., García-Hernández et al. 2010), assuming that the 9-13 μm carrier is related to HAC-like dust grains. However, fullerenes seem to coexist with the 9-13 μm carrier at the northeast outer regions of the nebula; something that could indicate that fullerenes may be attached to dust grains or well mixed with the 9-13 μm carrier. An alternative interpretation may be that fullerenes are not directly linked to the 9-13 μm carrier. Finally, another exciting interpretation (perhaps more consistent with the fullerene emission observed) is that other fullerene-based species are contributing to the observed 17.4 μm emission (see also Subsection 4.1); with ionized and/or more resistant fullerene-based species located in the inner regions near the central star and

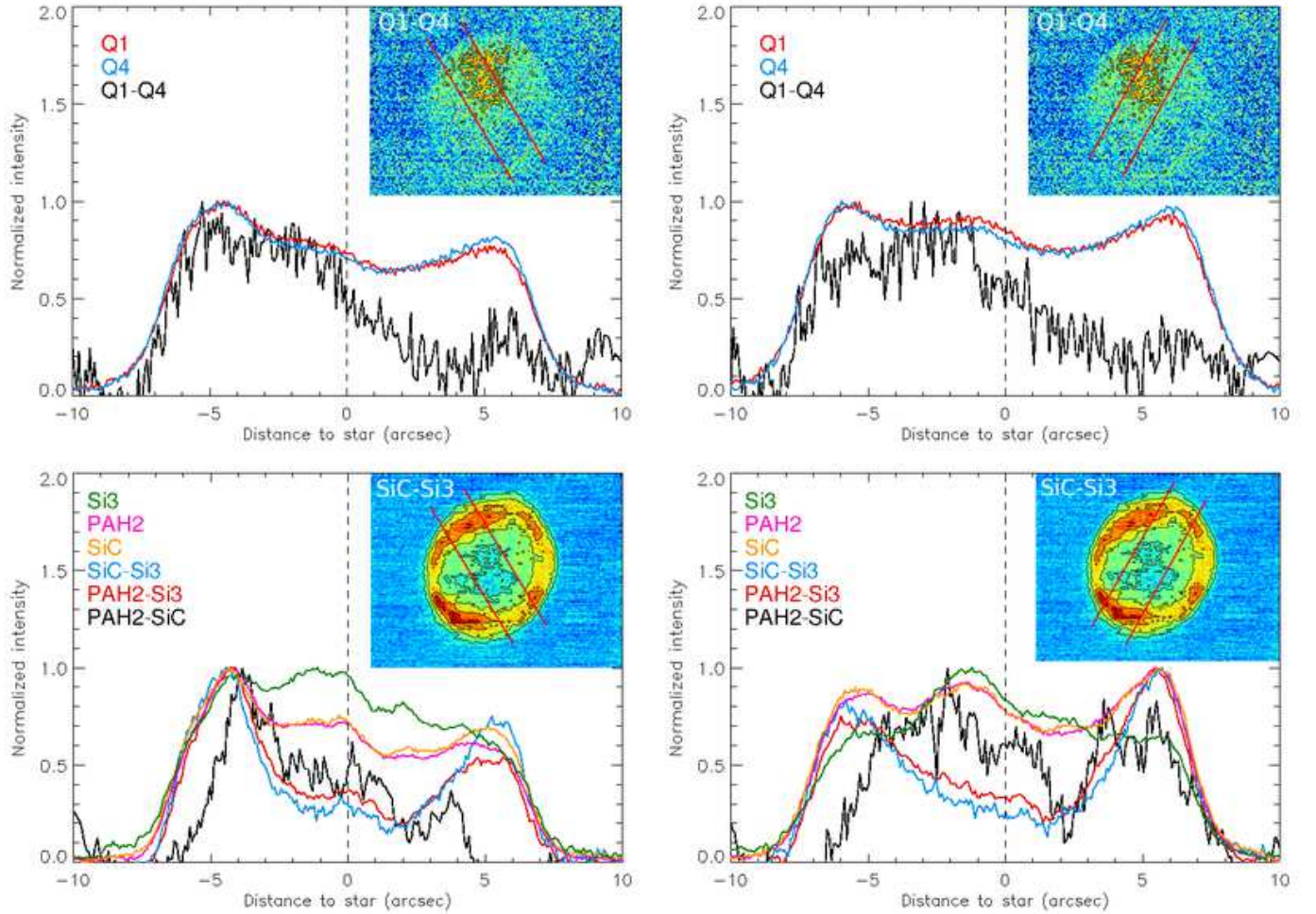


Figure 9. Normalized intensity profiles along the IC 418 nebula at P.A. of 70° (left panels) and 110° (right panels) from east as a function of the distance to the central star. The P.A. and the 4 arcsec width are indicated in the inset panels. The top panels show the intensity profiles in the Q1 (C_{60} + continuum at $17.65 \mu\text{m}$; in red), Q4 (continuum at $20.5 \mu\text{m}$; in blue), and continuum-subtracted Q1–Q4 (C_{60} ; in black) images. The lower panels show the intensity profiles in the Si3 (continuum at $9.8 \mu\text{m}$; in strong green), SiC and PAH2 (both containing $9\text{--}13 \mu\text{m}$ carrier + $11.3 \mu\text{m}$ PAH-like emission + continuum; in brown and pink, respectively), PAH2–SiC ($11.3 \mu\text{m}$ PAH-like emission; in black), and continuum-subtracted SiC–Si3 and PAH2–Si3 ($9\text{--}13 \mu\text{m}$ carrier + $11.3 \mu\text{m}$ PAH-like emission; in blue and red, respectively) images, which were calibrated using the synthetic photometry. The vertical dashed line marks the center of the nebula (or central star position).

neutral (and/or less resistant) fullerenes distributed in the outer ring-like structure. More complex fullerene-based species can emit at this wavelength. For example, laboratory IR spectra of fullerene-based species like fullerene-PAHs adducts display spectral features strikingly similar to those from C_{60} (and C_{70}) fullerenes (e.g., García-Hernández et al. 2013, 2016; Cataldo et al. 2014, 2015). Furthermore, a recent theoretical study of the vibrational modes of hydrogenated fullerenes (fulleranes; $C_{60}H_m$, $m=2\text{--}36$) shows that the four mid-IR bands (at ~ 7.0 , 8.5 , 17.4 , and $18.9 \mu\text{m}$) of the C_{60} -skeletal vibrations are stronger in fullerenes at low hydrogenation ($m=2\text{--}8$) and the astronomically observed IR bands assigned to C_{60} could be due to fullerenes/fulleranes mix-

tures (Zhang et al. 2017). Interestingly, most of $C_{60}H_m$ ($m=2\text{--}8$) display stronger emission features at $17.4 \mu\text{m}$ (i.e., higher $17.4 \mu\text{m}/18.9 \mu\text{m}$ band ratios) than C_{60} and fullerenes with very low H-content could potentially explain the intriguing spatial distribution of the residual $17.4 \mu\text{m}$ emission seen in IC 418. Indeed, the presence of fullerenes with very low H-content would be consistent with the non-detection of $\sim 3.4\text{--}3.6 \mu\text{m}$ emission bands in the fullerene-rich PNe Tc 1 and M 1-20 (Díaz-Luis et al. 2016); the strength of these fullerene bands depends on the number of active C-H bonds, being much stronger in the highly hydrogenated ones (Sadjadi 2017; priv. comm.; see also Zhang et al. 2017).

We note that our mid-IR images do not provide definitive proof about the dominant excitation mechanism of the fullerene emission (e.g., thermal or fluorescence emission); as it is also found in the literature (e.g., García-Hernández et al. 2012; Bernard-Salas et al. 2012; Otsuka et al. 2014; Brieva et al. 2016). Our observations may suggest that fullerenes could be attached to dust grains due to the considerable similarity between the spatial distribution of the IR emission in the Q1 and Q4 filters. In thermal excitation, fullerenes should closely follow the dust distribution and show a similar behaviour with respect to the distance to the central star. However, the temperature of thermally excited fullerene molecules in PNe range from ~ 200 to 600 K (e.g., García-Hernández et al. 2012) and it would be of only 33 K in IC 418 (Equation (3) in García-Hernández, Rao & Lambert 2012). Thus, the spatial distribution of fullerenes in IC 418 (as well as in Tc 1) could favor fluorescence excitation. Fluorescence models, on the contrary, cannot fully reproduce the emission of the fullerene IR bands in PNe and contamination of the C_{60} band strengths from UIR or other species like fullerene-clusters has been suggested (e.g., Bernard-Salas et al. 2012, 2013; Brieva et al. 2016). This would be consistent with the idea of other fullerene-based species like fullerenes with very low H-content emitting at $17.4 \mu\text{m}$, as tentatively suggested by the IC 418 mid-IR observations presented here (see above).

In short, our GTC/CanariCam observations of IC 418 thus show that higher sensitivity mid-IR images as well as spatially resolved mid-IR spectra along the nebula (e.g., using the upcoming James Webb Space Telescope, JWST) are needed in order to confirm the spatial distribution of the fullerene-, aromatic-, and aliphatic-like species and to learn about fullerene formation and excitation in the complex circumstellar environments around PNe.

6. SUMMARY/CONCLUSIONS

We have presented for the first time high spatial resolution (seeing-limited) narrow-band mid-IR images of a C_{60} -containing PN (IC 418); covering the fullerene band at $17.4 \mu\text{m}$, the PAH-like feature at $11.3 \mu\text{m}$, and the broad $9\text{--}13 \mu\text{m}$ aliphatic-like feature as well as their adjacent continua. We have studied the relative spatial distribution of these complex species with the main aim of getting some observational constraints on the formation process of fullerenes in the H-rich circumstellar environments around PNe.

A similar ring-like extended structure is seen in all narrow-band filters, with the exception of the dust continuum emission at $9.8 \mu\text{m}$, which peaks much closer

to the central star. The continuum-subtracted images show a clear ring-like extended emission structure for the broad $9\text{--}13 \mu\text{m}$ feature carrier, while only weak residual emission (at $\sim 4\text{--}5\sigma$ from the mean background level) is recovered for the PAH-like and fullerene emissions at 11.3 and $17.4 \mu\text{m}$, respectively. The $11.3 \mu\text{m}$ PAH-like emission seems to partially follow the ring-like structure seen at other wavelengths, while the $17.4 \mu\text{m}$ C_{60} -like emission is mainly located at the northeast, extending from the central star to the outer regions of the nebula.

The residual C_{60} emission, if real, might have several interpretations (not conclusive) regarding the dominant fullerene formation process in PNe. We speculate that other more complex fullerene compounds are likely contributing to the observed $17.4 \mu\text{m}$ emission. In this context, hydrogenated fullerenes with very low H-content seem to be potential candidates for the possible contaminants, which otherwise could explain the present inconsistency between the fullerene IR band ratios observed in PNe and the predictions of thermal/fluorescence excitation models as well as the lack of $\sim 3.4\text{--}3.6 \mu\text{m}$ emission features in fullerene-rich PNe.

We conclude that higher sensitivity mid-IR images and spatially resolved spectroscopic observations (e.g., by using the upcoming JWST) are necessary to confirm the spatial distribution of the fullerene-, aromatic-, and aliphatic-like species in fullerene-rich PNe. The JWST is thus the ideal astronomical facility to understand the formation and excitation of fullerenes in circumstellar environments.

We acknowledge Omaira González Martín for her help during the data reduction with RedCan. JJDL, DAGH, and AMT also acknowledge support provided by the Spanish Ministry of Economy and Competitiveness (MINECO) under grant AYA-2014-58082-P. DAGH was also funded by the Ramón y Cajal fellowship number RYC-2013-14182. EV acknowledges support from the Spanish Ministry of Economy and Competitiveness (MINECO) under grant AYA-2014-55840P. This work has been partially supported by MINECO grant AYA2016-78994-P.

Software: SMART (<http://isc.astro.cornell.edu/smart>), IRAF (Tody 1986, Tody 1993)

REFERENCES

- Alata, I. et al. 2014, *A&A*, 569, A119
- Álvaro Galué, H., & Díaz Leines, G. 2017, *Phys. Rev. Lett.*, 119, 171102
- Bernard-Salas, J., Cami, J., Peeters, E. et al. 2012, *ApJ*, 757, 41
- Bernard-Salas, J., Cami, J., Jones, A. et al. 2013, *Proceedings of The Life Cycle of Dust in the Universe: Observations, Theory, and Laboratory Experiments (LCDU2013)*, 32
- Berné, O., & Tielens, A. G. G. M. 2012, *Proceedings of the National Academy of Science*, 109, 401
- Berné, O., Montillaud, J., & Joblin, C. 2015, *A&A*, 577, A133
- Brieva, A. C., Gredel, R., Jager, C., Huisken, F., Henning, T. 2016, *ApJ*, 826, 122
- Cami, J., Bernard-Salas, J., Peeters, E., & Malek, S. E. 2010, *Science*, 329, 1180
- Campbell, E. K., Holz, M., Gerlich, D., & Maier, J. P. 2015, 523, 322
- Cataldo, F., García-Hernández, D. A., & Manchado, A. 2014, *Eur. Chem. Bull.*, 3, 740
- Cataldo, F., García-Hernández, D. A., & Manchado, A. 2015, *FNCN*, 23, 818
- Cutri, R. M. et al. 2013, *VizieR On-line Data Catalog: II/328*
- Díaz-Luis, J. J., García-Hernández, D. A., Manchado, A., Cataldo, F. 2016, *A&A*, 589, A5
- Feibelman, W. A. 1983, *ASP*, 95, 886
- Fulvio, D., Gobi, S., Jaeger, C., et al. 2017, *ApJS*, 233, 14
- García-Hernández, D. A., Manchado, A., García-Lario, P., et al. 2010, *ApJ*, 724, L39
- García-Hernández, D. A., Iglesias-Groth, S., Acosta-Pulido, J. A., et al. 2011a, *ApJ*, 737, L30
- García-Hernández, D. A., Rao, N. K., & Lambert, D. L. 2011b, *ApJ*, 729, 126
- García-Hernández, D. A., Villaver, E., García-Lario, P., et al. 2012, *ApJ*, 760, 107
- García-Hernández, D. A., Rao, N. K., & Lambert, D. L. 2012, *ApJ*, 759, L21
- García-Hernández, D. A., Cataldo, F., & Manchado, A. 2013, *MNRAS*, 434, 415
- García-Hernández, D. A., Cataldo, F., & Manchado, A. 2016, *FNCN*, 24, 679
- Goeres, A., & Sedlmayr, E. 1992, *A&A*, 265, 216
- González-Martín, O., Díaz-Santos, T., Rodríguez-Espinosa, J. M., et al. 2013, *Fourth Science Meeting with the GTC, Revista Mexicana de Astronomía y Astrofísica*, 42, 118
- Helou, G., & Walker, D. W., eds. 1988, *Infrared astronomical satellite (IRAS) catalogs and atlases. Volume 7: The small scale structure catalog, Vol. 7, 1*
- Ishihara, D., Onaka, T., Kataza, H., et al. 2010, *A&A*, 514, A1
- Jäger, C., Huisken, F., Mutschke, H., Jansa, I. L., & Henning, Th. 2009, *ApJ*, 696, 706
- Kwok, S., & Zhang, Y. 2011, *Nature*, 479, 80
- Li, A., & Draine, B. T. 2012, *ApJL*, 760, L35
- Manchado, A. 2004, in *Astronomical Society of the Pacific Conference Series, Vol. 313, Asymmetrical Planetary Nebulae III: Winds, Structure and the Thunderbird*, ed. M. Meixner, J. H. Kastner, B. Balick, & N. Soker, 3
- Micelotta, E. R., Jones, A. P., Cami, J., et al. 2012, *ApJ*, 761, 35
- Morisset, C., & Georgiev, L. 2009, *A&A*, 507, 1517
- Otsuka, M., Kemper, F., Cami, J., et al. 2014, *MNRAS*, 437, 2577
- Pottasch, S. R., Bernard-Salas, J., Beintema, D. A., et al. 2004, *A&A*, 423, 593
- Ramos-Larios, G., Vázquez, R., Guerrero, M. A., et al. 2012, *MNRAS*, 423, 3753
- Scott, A., Duley, W. W., & Pinho, G. P. 1997, *ApJ*, 489, L193
- Sellgren, K., Werner, M. W., Ingalls, J. G., et al. 2010, *ApJ*, 722, L54
- Taylor, A. R., & Pottasch, S. R. 1987, *A&A*, 176, L5
- Taylor, A. R., Gussie, G. T., & Goss, W. M. 1989, *ApJ*, 340, 932
- Telesco, C. M., Ciardi, D., French, J., et al. 2003, *Instrument Design and Performance for Optical/Infrared Ground-based Telescopes, Proceedings of the SPIE*, 4841, 913
- Tielens, A. G. G. M. 2011, *EAS Publications Series*, 46, 3
- van Dokkum, P. G., Franx, M., Kelson, D. D., & Illingworth, G. D. 2001, *ApJ*, 553, L39
- Walker, G. A. H., Bohlender, D. A., Maier, J. P., Campbell, E. K. 2015, *ApJ*, 812, L8
- Zhang, Y., & Kwok, S. 2011, *ApJ*, 730, 126
- Zhang, Y., & Kwok, S. 2015, *ApJ*, 798, 37
- Zhang, Y., Sadjadi, S., Hsia, C.-H., Kwok, S. 2017, *ApJ*, 845, 76
- Zhen, J. et al. 2014, *ApJ*, 797, L30